Check for updates

Coupling effect of reaction conditions on the catalytic activity of Cu–Mn composite oxide catalysts for toluene

Yungang Wang, [ID] [a] Xu Liang,[a] Yanjun Dai,*[a] Li Zou,[a] Dou Sun[a] and Feixiang Li*[b]

Volatile organic compounds (VOCs) are one of the major components of air pollution. Catalytic combustion is a promising technology for the treatment of VOCs and at its center is the preparation of efficient and cheap catalysts. In this study, by loading copper (Cu) and manganese (Mn) on Santa Barbara Amorphous-15 (SBA-15) molecular sieve, the $Cu_x–Mn_y$/SBA-15 (x = 1, 2; y = 1, 2) composite metal oxide catalyst was prepared using the equal volume impregnation method. Their performance in the toluene catalytic combustion reaction was investigated by adjusting the molar ratio (x : y), and the loading of Cu and Mn. The results of the Brunner–Emmett–Teller (BET), X-ray diffraction (XRD), scanning electron microscopy (SEM), and X-ray photoelectron spectroscopy (XPS) analyses show that the CuMnO spinel phase can be detected in the Cu–Mn composite metal oxide catalyst doped with a low concentration of Cu. The overall rod-like structure of the fibrous network structure provides a large specific surface area, and the particle crystallinity is low and the dispersion is good. Due to the synergistic effect of Cu and Mn, the greater the amount of Mn^{3+} and adsorbed oxygen species (O_{ads}) that are available, and the higher the turnover frequency (TOF) value, the better and more superior catalytic performance and excellent stability is obtained, when compared with the single-component oxides used in toluene catalytic combustion. After a continuous catalytic reaction for 12 h, the toluene conversion rate remained above 95%. The coupling effect of the catalytic reaction temperature and concentration of oxygen on the catalytic combustion of toluene was also studied. At a low reaction temperature (<250 °C), the increase of the concentration of oxygen played a superior role in promoting the conversion of toluene. The kinetic analysis of the toluene catalytic combustion process showed that the catalytic combustion of toluene by Cu–Mn/SBA-15 followed both the Mars–Van Krevelen (MVK) and Langmuir–Hinshelwood (L–H) reaction mechanisms. With the increase of the O_{ads} amount caused by the decrease of the Cu ratio, the proportion of the L–H reaction mechanism increases.

1. Introduction

Organic compounds involved in atmospheric photochemical reactions are known as volatile organic compounds (VOCs).[1] As important precursors of photochemical smog and fine particulate matter ($PM_{2.5}$),[2] VOCs not only induce haze and pollute the atmosphere, but also damage human health and biological growth.[3] The VOCs treatment technologies include adsorption, condensation, catalytic combustion, photocatalysis, non-thermal plasma methods, and so on.[4–8] For catalytic combustion technology, the final major products are harmless carbon dioxide (CO_2) and water. It has become one of the most promising treatment technologies due to its low energy consumption and high efficiency.[9,10]

Catalysts consist of an active component and a carrier, and depending on the active component, they can be classified as noble metal catalysts (Au, Pd, Pt, and so on)[11–13] and transition metal catalysts (Co, Cu, Mn, and so on).[7,14] Although the noble metal catalysts have a high catalytic activity at low temperatures, the properties of unsustainability, high cost, and susceptibility to sintering and carbon deposition, restrict their wide application in industry.[15] The development of non-noble metal catalysts with a high catalytic activity has become the focus of research. Among them, the Cu and Mn oxides became the focus of current research because of their high catalytic activity and high stability.[16,17] The Mn-based catalysts have an excellent catalytic performance due to the double exchange behaviour between the Mn^{3+} and Mn^{4+} that can promote electron transfer.[18] Adding other metals to the Mn oxide catalyst to form a composite catalyst can improve its performance, but it does not mean the higher the ratio, the better the performance. The

[a]Key Laboratory of Thermo-Fluid Science and Engineering (Ministry of Education), Xi'an Jiaotong University, Xi'an 710049, Shaanxi, China. E-mail: daiyanjun2015@xjtu.edu.cn

[b]Hubei Special Equipment Inspection and Testing Institute, Wuhan, 430077, China. E-mail: 26005838@qq.com

main drawback of metal oxide catalysts is their tendency to deactivate due to aggregation. Therefore, they can be supported on a carrier to improve their dispersion. The carriers primarily include Al_2O_3, SiO_2, activated carbon, and molecular sieves.[19–22] Among them, mesoporous molecular sieves have the potential to generate well-dispersed and stable metal particles, thereby offering further enhancement of the catalytic activity of the metal oxide catalysts. The molecular sieve, SBA-15 has gained extensive attention due to its regular hexagonal pore arrangement, uniform pore size, extremely high surface area, and large pore volume. It also exhibits inertness and stability at high temperatures, as well as good mechanical stability.[9,10] Appropriate loading is also an important factor affecting catalyst activity.

Various reaction conditions, such as reaction temperature, space velocity, toluene concentration, and so on, remarkably effect the efficiency of the VOCs catalytic combustion.[23–25] However, there are few studies on the impacts of concentration of oxygen in the reaction gas and the coupling with other reaction conditions, on the VOCs catalytic combustion. Hu et al.[24] examined the toluene catalytic combustion over a Cu/MnO catalyst with toluene gas switched with oxygen and nitrogen ($O_2 : N_2 = 1 : 4$). In the same method that other researchers used to explore the catalytic combustion of toluene, the reaction gas was also a mixture of nitrogen and oxygen with a fixed proportion.[26,27] In addition, the reaction of toluene gas in catalytic combustion with nitrogen was investigated by Wang et al.[25] In related studies, the effect of the concentration of oxygen on the catalytic combustion of toluene was not studied. Oxygen plays a vital role in the catalytic combustion of toluene, and a low concentration of oxygen will lead to insufficient combustion of toluene gas and reduce the removal rate. An excessive content will increase the treatment cost. In actual industrial production, the appropriate concentration of oxygen can be selected, according to different reaction conditions, to achieve the highest toluene removal rate at the minimum energy consumption. Based on the previous analysis, the impacts of the concentration of oxygen in the reaction gas and coupling with other reaction conditions on VOC catalytic oxidation is investigated extensively in the research discussed in this paper, especially when non-precious metal catalysts are selected to catalyze oxidation. The results can provide a reference for the design and optimization of catalysts, reaction systems, and reaction parameters in industrial processes. This is significant for the development of more efficient and sustainable processes for the combustion of VOCs.

As a consequence, the present paper is focused on exploring the catalytic combustion characteristics and reaction mechanism of VOCs under different reaction temperatures and concentrations of oxygen. The Cu–Mn/SBA-15 catalysts with various loadings and different relative contents of Cu/Mn were synthesized using the equal volume impregnation method. The effects of the catalyst active components and reaction conditions on the catalytic combustion of the VOCs were explored in a fixed bed reactor with toluene as a molecular probe, and a stability test was carried out. The catalysts were characterized using BET, XRD, SEM and XPS. Combined with kinetic analysis,

the catalytic combustion mechanism of toluene on the Cu–Mn/SBA-15 was proposed. This study aimed to provide a low-cost and efficient non-precious metal composite oxide catalyst, and to explore its coupling effect under different reaction conditions, to promote the development of the VOC's removal technology.

2. Experimental

2.1 Materials

Manganese nitrate solution (50% $Mn(NO_3)_2$), copper nitrate trihydrate ($Cu(NO_3)_2 \cdot 3H_2O$), quartz sand, toluene and ethanol were purchased as AR from Sinopharm Chemical Reagent Company. Nitrogen (99.99%) and oxygen (99.99%) were procured from the Xi'an Tenglong Chemical Company.

The Cu–Mn/SBA-15 samples were prepared using the impregnation method. Firstly, a specific amount of SBA-15 was soaked in an aqueous mixture of $Cu(NO_3)_2$ and $Mn(NO_3)_2$ with constant stirring. After keeping the mixture at room temperature (ca. 25 °C) for 12 h, the products were then dried at 110 °C for 12 h. Then these products were calcined in air for 4 h at 400 °C. Using the previous steps, the Cu and Mn were loaded onto the SBA-15 carrier Cu_1Mn_1/SBA-15 with loadings of 10%, 20%, 30%, 40% and 50%. For Cu_1Mn_2/SBA-15 and Cu_2Mn_1/SBA-15, only samples with a 40% loading were prepared. Abbreviation and detailed experimental conditions of the Cu–Mn/SBA-15 samples are shown in Table 1. In Table 1, 'Cu_1Mn_2' indicates that the molar ratio of Cu to Mn is 1 : 2, and so on.

2.2 Instrumental measurements

The textural characteristics of the samples were determined from the adsorption isotherm of N_2 at −196 °C which was obtained using an ASAP 2020 Plus HD88 (Micromeritics) automatic physical adsorption instrument. All the samples were heat-treated at 150 °C under vacuum overnight before the analysis.

The XRD patterns were obtained by using an XRD-6100 (Shimadzu, Japan) instrument, with Cu-Kα radiation ($\lambda = 1.5418$ Å), focusing geometry θ–2θ in the scanning mode within a range of angles of 2θ from 10° to 80° with a step of 0.02°.

Table 1 Abbreviations and experimental conditions of for obtaining Cu–Mn/SBA-15 samples

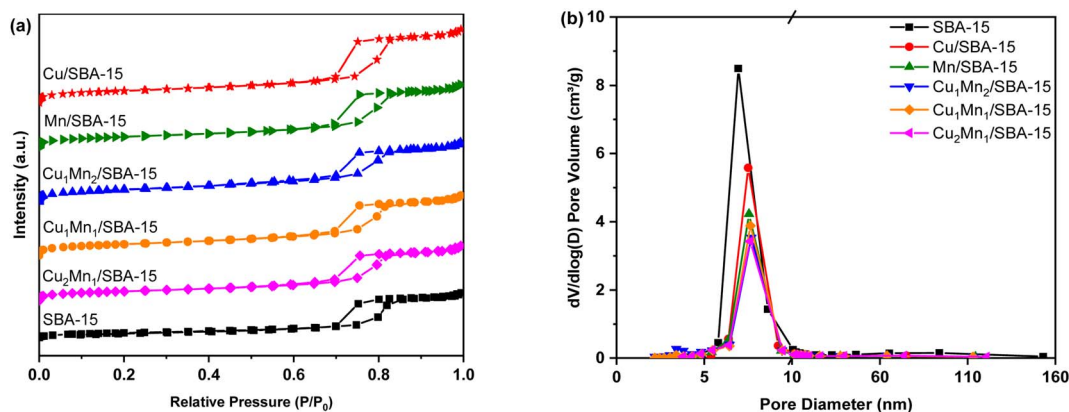| Abbreviation	Loading of active components (wt%)	Metal content (wt%)	
		Cu	Mn
Cu/SBA-15	40	40	0
Mn/SBA-15	40	0	40
Cu_1Mn_2/SBA-15	40	14.7	25.3
Cu_1Mn_1/SBA-15	10	5.4	4.6
Cu_1Mn_1/SBA-15	20	10.7	9.3
Cu_1Mn_1/SBA-15	30	16.1	13.9
Cu_1Mn_1/SBA-15	40	21.5	18.5
Cu_1Mn_1/SBA-15	50	26.8	23.2
Cu_2Mn_1/SBA-15	40	27.9	12.1

Fig. 1 (a) The N$_2$ adsorption–desorption isotherms, and (b) pore-size distribution.

The surface morphology was observed using field-emission scanning electron microscopy (FE-SEM) with a Gemini 500 instrument (Zeiss, Germany).

The XPS using an Axis Ultra DLD (Kratos, UK) was adopted for determining the elemental composition and chemical states.

2.3 Catalytic combustion experiments

A fixed-bed reactor (inner diameter = 20 mm) was utilized to conduct the toluene catalytic combustion experiments. For each experiment, 0.1 g of catalyst and 0.9 g of quartz sand were weighed and evenly mixed before being placed into the reactor. With a toluene concentration of 1500 mg m^{-3}, the total rate of the gas mixture (N$_2$ and O$_2$) was 200 mL min^{-1} with a weight hourly space velocity (WHSV) of 12 000 mL g^{-1} h^{-1}. The volume concentration of the oxygen was changed by changing the oxygen flow rate. Each set of experiments was performed for 30 min under various reaction conditions. The toluene concentration was monitored using a toluene gas detector. Each set of experiments was performed for 30 min under various reaction conditions and repeated three times to determine the average toluene concentration. The toluene conversion was calculated using eqn (1):

$$\eta = \frac{C_{in} - C_{out}}{C_{in}} \times 100\% \qquad (1)$$

where C_{in} and C_{out} are the toluene concentrations at the inlet gas and at the outlet gas, respectively.

3. Results and discussion

3.1 Catalyst characterization

3.1.1. Specific surface area and pore structure. The N$_2$ adsorption–desorption isotherms and pore size distributions of the catalysts are shown in Fig. 1. All the catalysts exhibited type IV adsorption isotherms and type H1 hysteresis loops, demonstrating that capillary condensation occurred in the pores. The range and uniformity of the pore size distribution can be observed from the position and shape of the hysteresis loops.[28] The pore sizes of all catalysts were concentrated in range of 5–

10 nm, which suggested that the materials exhibited a mesoporous structure. As shown in Table 2, the loading of active components did not change the mesoporous structure of SBA-15, and the pore diameter of the catalysts was approximately 8 nm. However, the specific surface area and pore volume of the catalysts were affected in a remarkable manner by the loading of the active components. Among the catalysts obtained, the Cu$_1$Mn$_2$/SBA-15 displayed the maximum specific surface area (268 m^2 g^{-1}) with a pore volume of 0.52 cm^3 g^{-1}. Large specific

Table 2 Specific surface areas, pore volumes and pore diameters of different catalysts

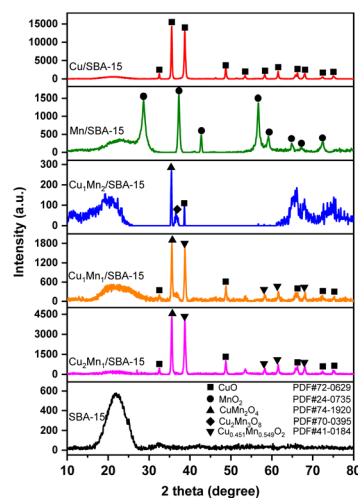| Sample	BET surface area (m^2 g^{-1})	Pore volume (cm^3 g^{-1})	Pore diameter (nm)
SBA-15	309	1.13	8.03
Cu/SBA-15	260	0.64	8.12
Mn/SBA-15	240	0.55	8.36
Cu$_1$Mn$_2$/SBA-15	268	0.52	7.64
Cu$_1$Mn$_1$/SBA-15	250	0.53	8.26
Cu$_2$Mn$_1$/SBA-15	209	0.48	8.39

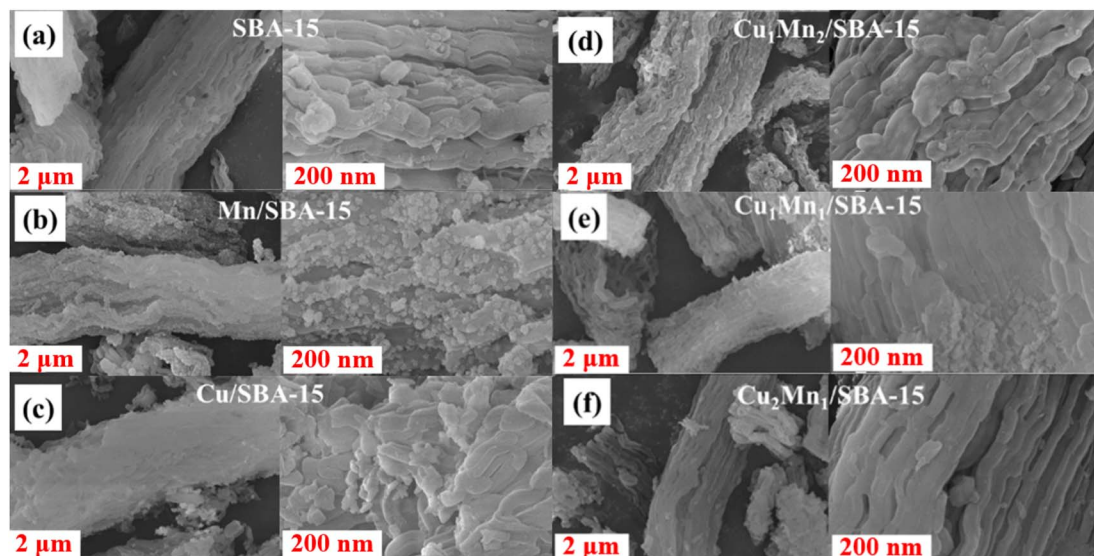**Fig. 2** The XRD patterns of different catalysts.

Fig. 3 (a–f) SEM images of different catalysts.

surface areas can improve the availability of active sites in the catalytic reaction, as well as improving the catalytic efficiency.[29]

3.1.2. Crystal structure. Fig. 2 shows the XRD patterns of various catalysts. A broad diffraction peak assigned to amorphous silica is observed in the 2θ range from $20°$ to $25°$, for the pristine SBA-15 sample.[30] The Cu/SBA-15 consists mainly of CuO, whereas the Mn/SBA-15 consisted mainly of MnO_2. Compared with single-component catalysts, the Cu–Mn/SBA-15 also has a CuMnO spinel phase, which contributes to the increase of the activity and stability.[27,31] Furthermore, the XRD patterns of the Cu–Mn/SBA-15 with various Cu/Mn molar ratios demonstrated that there was an extremely low diffraction peak intensity of the metal oxides in Cu_1Mn_2/SBA-15. This finding suggested that the grains of the active components in Cu_1Mn_2/SBA-15 were tiny and consistently distributed on the support, which was conducive for toluene catalytic combustion.[32]

3.1.3. Micromorphology. The SEM was adopted to characterize the morphology and structure of different catalysts, and the images obtained are shown in Fig. 3a–f. The catalyst has an integral rod shape with a fibrous network structure. The overall structure of SBA-15 was unaffected by the loading of active components (Fig. 3a). However, the surface microstructure and morphology of the catalysts showed great differences because of the different loadings of the active components. The Mn nanoparticles of different sizes and shapes spread over the surface of SBA-15 with a fiber network structure in Mn/SBA-15 (Fig. 3b), whereas the active components of Cu/SBA-15 and Cu–Mn/SBA-15 (Fig. 3c) were greatly dispersed in the mesoporous channels of SBA-15. Compared with Cu_1Mn_2/SBA-15 (Fig. 3d), both Cu_1Mn_1/SBA-15 (Fig. 3e) and Cu_2Mn_1/SBA-15 (Fig. 3f) displayed different degrees of particle agglomeration, resulting in an increase in crystallinity and a reduction in specific surface area, as was also confirmed by the XRD and BET results. In addition, the elemental distribution of the Cu_1Mn_2/SBA-15 catalyst suggested that Cu, Mn and O were evenly separated on the catalyst surface as shown in Fig. 4.

3.1.4. Surface chemical status. Fig. 5a shows the XPS full spectra of different catalysts, and it was concluded that the catalysts were composed of Cu, Mn, O, and Si. The Cu 2p XPS spectra of various catalysts are shown in Fig. 5b. The binding energy of 953 eV was attributed to Cu^+. The peaks with binding energies of 942 and 934 eV were assigned to Cu_A^{2+} (tetrahedral site) and Cu_B^{2+} (octahedral site).[33] The Cu^{2+} was the main valence state and Cu^+ was derived from the partial reduction of Cu^{2+} in the reaction of $Cu^{2+} + Mn^{3+} = Cu^+ + Mn^{4+}$.[34] The XPS spectra of Mn 2p are shown in Fig. 5c. The binding energies within the range of 635–660 eV were assigned to the main peaks of Mn $2p_{1/2}$ and Mn $2p_{3/2}$. The peaks of Mn $2p_{1/2}$ corresponded to Mn^{3+} and Mn^{2+} at 653 and 650 eV, respectively, whereas the Mn $2p_{3/2}$ had a peak at 642 eV, which corresponded to Mn^{4+}. Fig. 5d shows the XPS spectra of O 1s. The adsorbed oxygen species (O_{ads}) and lattice
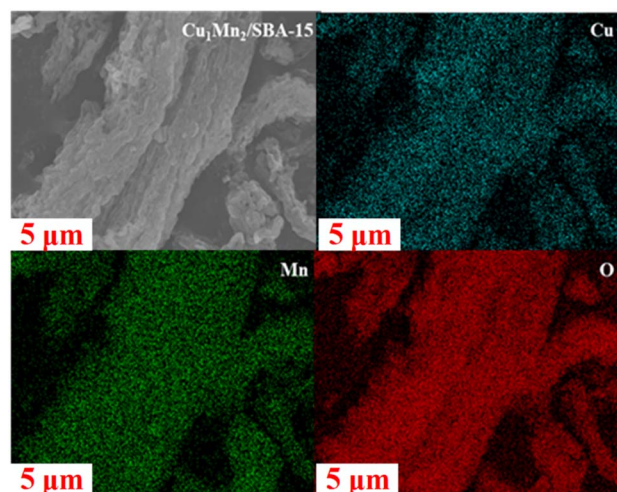

Fig. 4 The energy dispersive X-ray spectroscopy (EDS) distribution of Cu_1Mn_2/SBA-15.
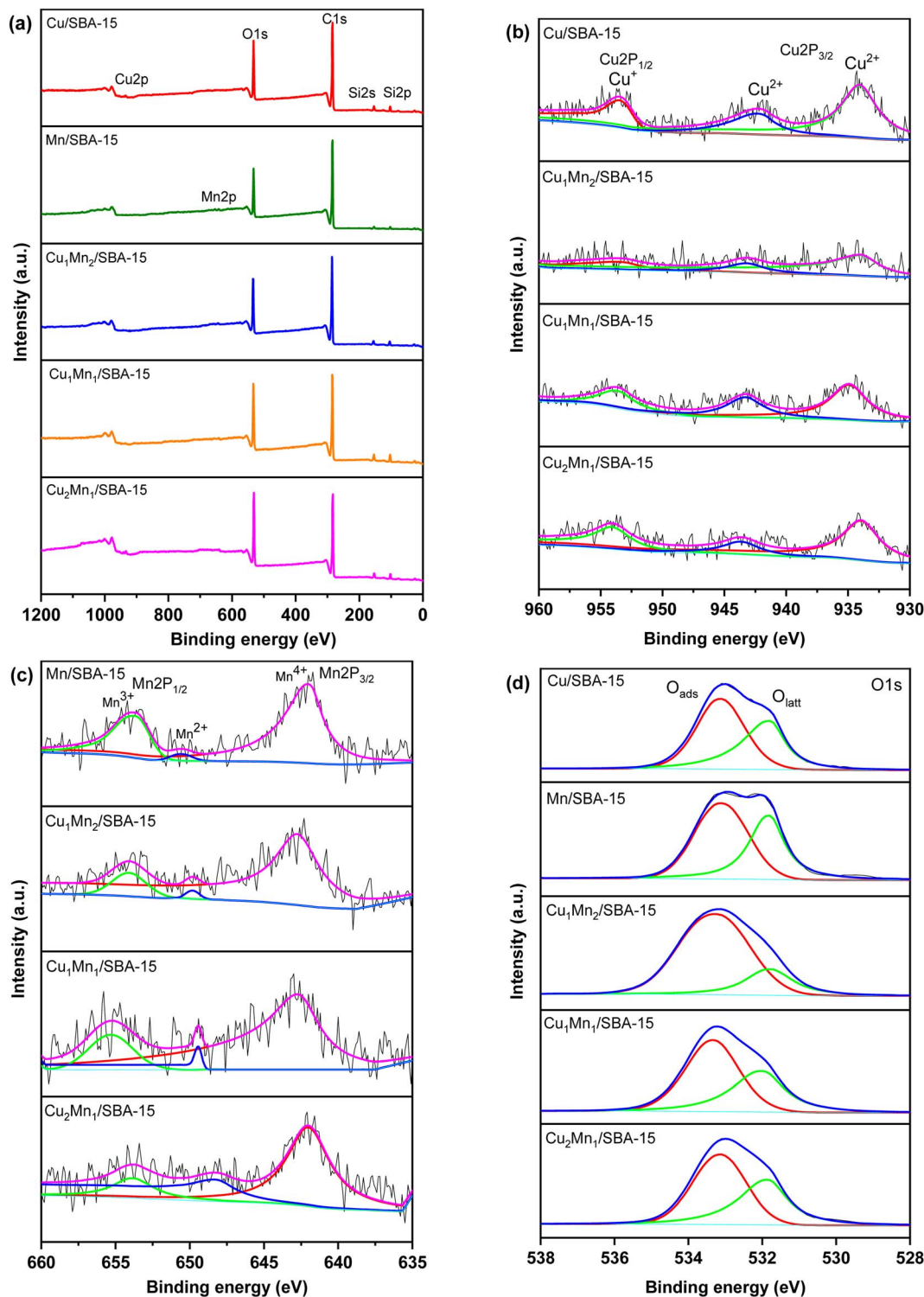
Fig. 5   (a) The XPS spectra, (b) Cu 2p, (c) Mn 2p, and (d) the O 1s XPS spectra of different catalysts.

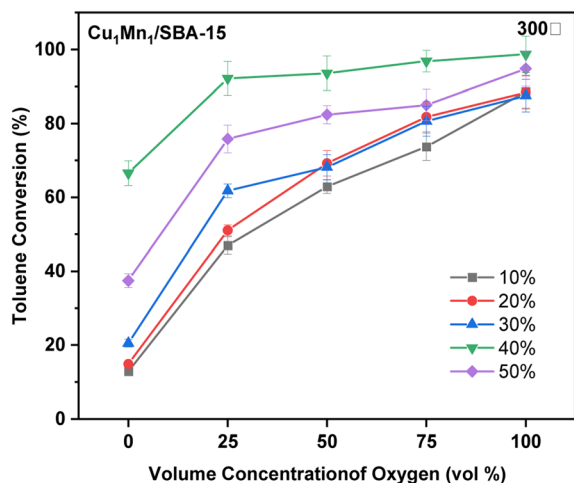oxygen species (O_{latt}) had the binding energies of 533 and 531 eV, respectively.

Table 3 shows the XPS results of the different catalysts. The Cu_1Mn_2/SBA-15 sample had more Mn^{3+} and a larger O_{ads} than Cu_1Mn_1/SBA-15 and Cu_2Mn_1/SBA-15. The greater the O_{ads} in the catalysts, the more oxygen vacancies and active species on the

surface of catalysts there were, which made it more favorable for toluene catalytic combustion.[26,34] A higher Mn^{3+} concentration was favorable for generating more oxygen vacancies, which could improve the catalytic activity and redox performance.[35] The crystallinity of the catalysts continuously increased with the increase in O_{latt} concentration. The variation in the O_{latt} concentration of

Table 3 The XPS results for different catalysts

Sample	Cu⁺ (%)	Cu²⁺ (%)	Mn³⁺ (%)	Mn⁴⁺ (%)	Mn²⁺ (%)	O_latt (%)	O_ads (%)
Cu_1Mn_2/SBA-15	20.88	79.12	25.99	56.50	17.51	24.81	75.19
Cu_1Mn_1/SBA-15	24.04	75.96	22.76	68.97	8.28	36.31	63.69
Cu_2Mn_1/SBA-15	29.63	70.37	16.34	65.36	18.30	39.02	60.98

Fig. 6 The effect of catalyst loading on toluene conversion (Cu_1Mn_1/SBA-15, T = 300 °C).

different catalysts indicated that the Cu_2Mn_1/SBA-15 had the highest crystallinity amongst the samples, which was compatible with the XRD characterization results.

3.2 Catalytic activity

3.2.1. Effect of catalyst loading. The toluene conversion plots of Cu_1Mn_1/SBA-15 under various loadings and

concentrations of oxygen at a reaction temperature (T) of 300 °C are shown in Fig. 6. The toluene removal efficiency of different catalysts constantly increased as the concentration of oxygen increased at the same loading. The toluene conversion of the catalyst reached the maximum when the catalyst loading was 40% under the same concentration of oxygen. Moreover, the
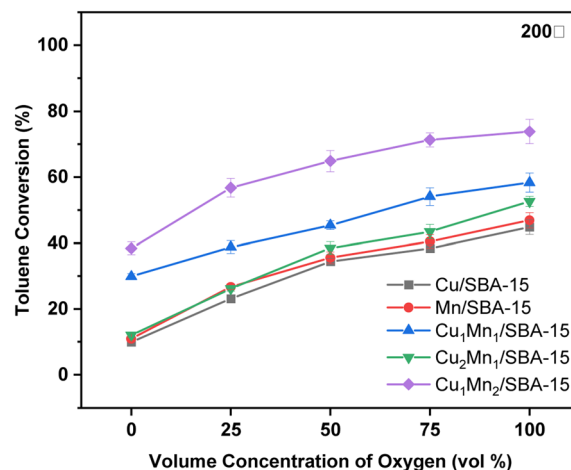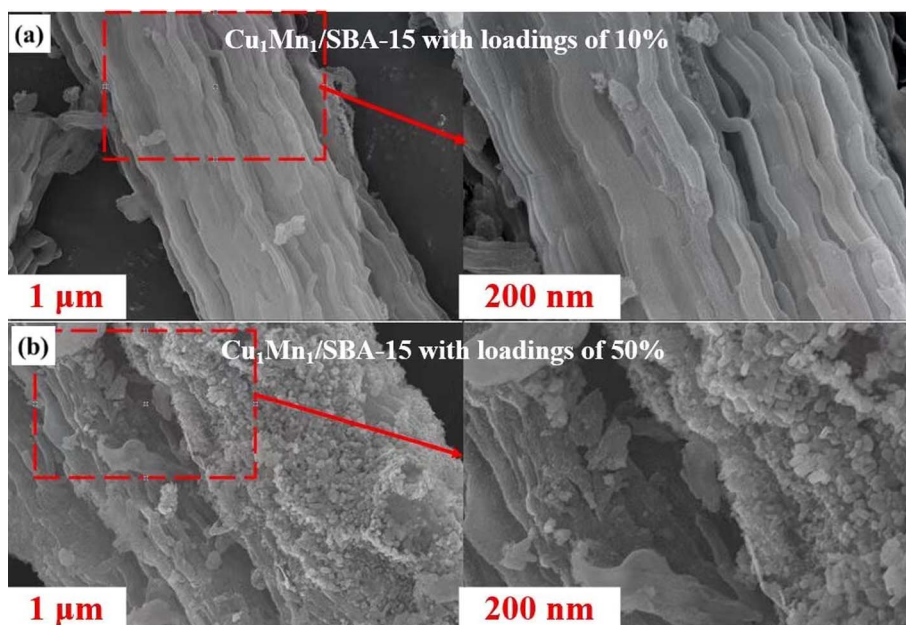

Fig. 8 The effect of single-component and multi-component catalysts on toluene removal efficiency.

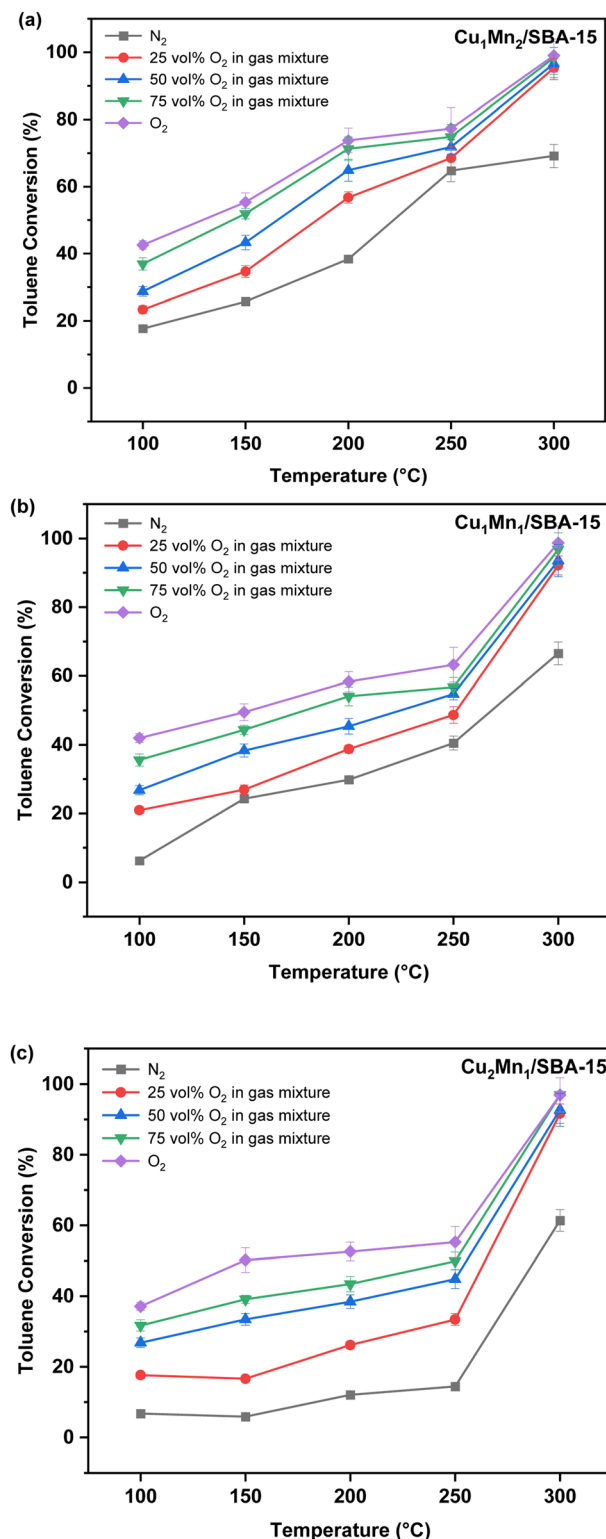**Fig. 7** The SEM images of Cu_1Mn_1/SBA-15 catalysts with different loadings.

Fig. 9 The effects of temperature and concentration of oxygen on toluene removal efficiency: (a) Cu_1Mn_2/SBA-15, (b) Cu_1Mn_1/SBA-15, (c) Cu_2Mn_1/SBA-15.

Fig. 10 Effect of the Cu/Mn mole ratio on toluene removal efficiency.

Fig. 11 Stability of the Cu_1Mn_2/SBA-15 catalyst.

toluene conversion was as high as 92.16% when the concentration of oxygen was 25 vol%. The lesser catalyst loading resulted in fewer active sites and a low catalyst efficiency. Fig. 7
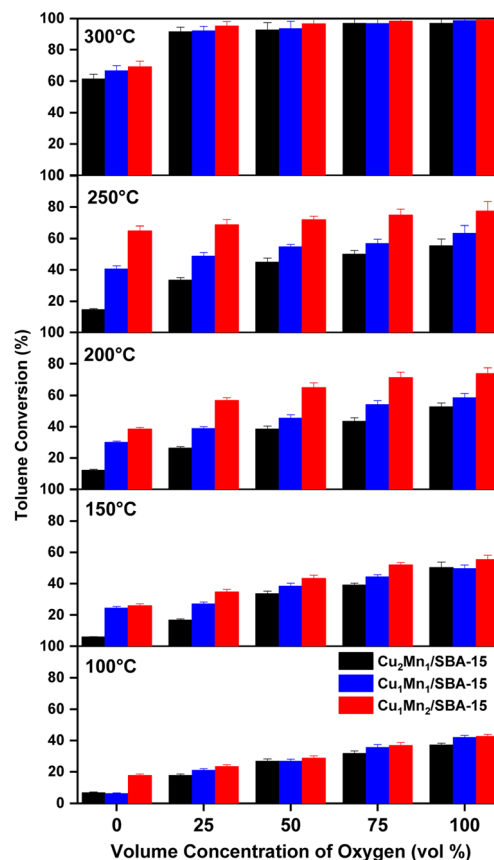
shows the SEM images of the Cu_1Mn_1/SBA-15 catalysts with different loadings. Compared to the catalyst with a loading of 10%, the catalyst with a loading of 50% showed particle agglomeration of the active component. Although the number of active sites increased with the increase of the loading amount, when the loading amount reached a certain level, continuing to increase the loading amount would not improve the catalytic activity. The reason for this is that excessive loading
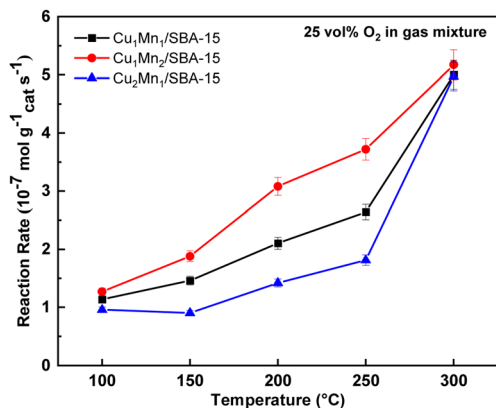
Fig. 12 Reaction rates of catalysts at different temperatures (25 vol% O_2 in gas mixture).

will cause the aggregation of active sites, thereby reducing the catalytic activity. Therefore, the optimal loading of catalyst was determined to be 40%, and this loading was adopted in subsequent experiments.

3.2.2. Effect of single-component and multi-component catalysts. Fig. 8 shows the toluene conversion curves of the single-component and multi-component catalysts at 200 °C. It can be seen that the two-component catalysts showed a better toluene conversion when compared with the single-component catalysts under the same reaction conditions. In particular, there was maximum toluene conversion and excellent low temperature catalytic combustion activity with Cu_1Mn_2/SBA-15. The XRD and SEM results indicated that the active component of Cu/SAB-15 had large crystal grains and uneven distribution, which resulted in particle agglomeration, thus the catalytic activity was also poor. The Cu–Mn/SBA-15 had more ionic species with different valences and higher oxygen concentrations than Cu/SBA-15 and Mn/SBA-15 because of the synergy between the different active components. Therefore, the Cu–Mn/SBA-15 demonstrated better catalytic activity.[26,36,37]

3.2.3. Effects of temperature and concentration of oxygen. Fig. 9 shows the toluene conversion plots of Cu–Mn/SBA-15 with different Cu/Mn molar ratios under different reaction

temperatures and concentrations of oxygen. The toluene removal efficiency constantly increased with the increase of reaction temperature and concentration of oxygen. In particular under the lower reaction temperature (<250 °C), the increase of concentration of oxygen significantly improved the toluene conversion. The toluene conversion of the Cu_1Mn_2/SBA-15 was increased by 18.4% when the concentration of oxygen was increased from 0 to 25 vol% at 200 °C. Notably, the toluene conversion of each sample exceeded 95% when the reaction temperature was 300 °C except in a pure nitrogen atmosphere. However, the increase in concentration of oxygen at 300 °C had a small influence on the toluene conversion. The effects of an increased concentration of oxygen on toluene conversion were significant under low reaction temperatures. Therefore, an appropriate concentration of oxygen can be selected according to different reaction temperatures to improve toluene conversion. When the reaction temperature was relatively low, increasing the concentration of oxygen was a primary means to upgrade the toluene removal efficiency.

When the temperature was lower than 250 °C, the toluene conversion of the Cu_2Mn_1/SBA-15 increased slightly with the increasing reaction temperature unlike those of the Cu_1Mn_1/SBA-15 and Cu_1Mn_2/SBA-15. When the reaction temperature was raised from 100 to 250 °C, the toluene removal efficiency only increased by 7.7% at 100 vol% N_2. However, the toluene removal efficiency increased by 46.9% when the reaction temperature was increased from 250 to 300 °C, which was attributed to the high content of O_{latt} in the Cu_2Mn_1/SBA-15. The reaction temperature of O_{latt} was higher in the absence of oxygen.[36]

3.2.4. Effect of the Cu/Mn mole ratio. Fig. 10 shows the effects of the Cu/Mn mole ratio of the catalysts on toluene conversion at different reaction temperatures, where the rate of the gas mixture was 200 mL min^{-1}. The order of the catalytic performance was Cu_1Mn_2/SBA-15 > Cu_1Mn_1/SBA-15 > Cu_2Mn_1/SBA-15. At reaction temperatures of 100 °C or 300 °C, catalysts with different Cu/Mn molar ratios showed little difference in removal efficiencies of toluene under the same oxygen flow rates. This was because temperature is the dominant factor affecting the reaction under these experimental conditions.
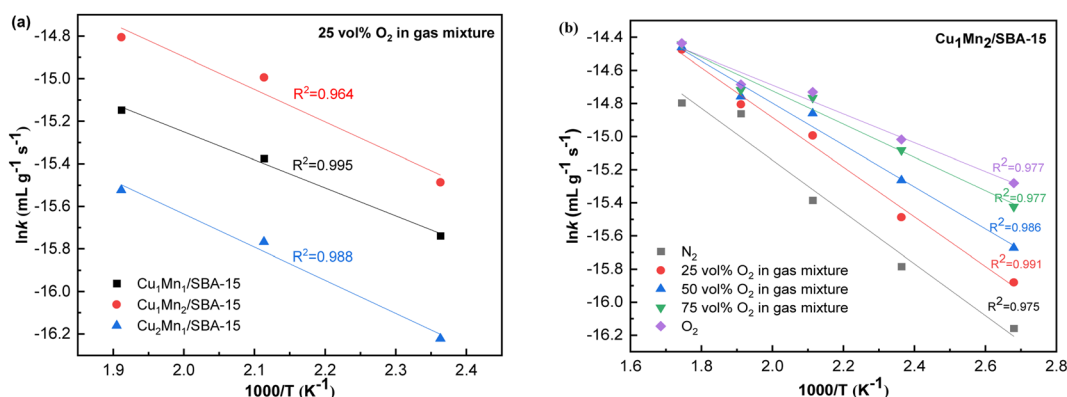

Fig. 13 Arrhenius plots of toluene combustion: (a) Arrhenius plots for different Cu/Mn molar ratio catalysts (25 vol% O_2 in gas mixture), (b) Arrhenius plots of Cu_1Mn_2/SBA-15 at different concentrations of oxygen (rate of gas mixture was 200 mL min^{-1}).

Table 4 Calculation of activation energy, reaction rate and TOF for different Cu/Mn molar ratio catalysts

Sample	$E_a{}^a$ (kJ mol^{-1})	R^{2b}	k^c (10^{-7} mol g$_{cat}{}^{-1}$ s^{-1})	TOF$_{Cu}{}^b$ (10^{-5} s^{-1})	TOF$_{Mn}{}^b$ (10^{-5} s^{-1})
Cu$_2$Mn$_1$/SBA-15	13.0	0.988	0.37	0.83	1.68
Cu$_1$Mn$_1$/SBA-15	11.7	0.964	0.34	1.00	1.00
Cu$_1$Mn$_2$/SBA-15	10.2	0.995	0.96	4.15	2.08

[a] The apparent activation energy (E_a) was calculated at 25 vol% O$_2$. [b] R^2 is an indicator to evaluate the quality of the regression model, *i.e.*, the degree of fit between the regression line and the experimental data points. [c] The reaction rates (k) and TOF calculations were at the experimental conditions of 100 °C and 100 vol% N$_2$ for catalytic combustion.
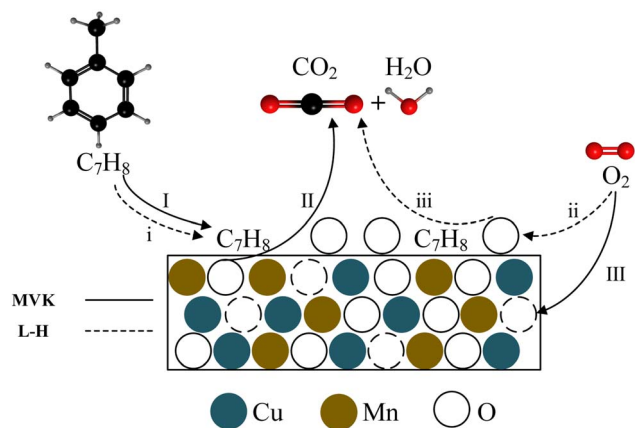

Fig. 14 Reaction mechanism of toluene on the Cu–Mn/SBA-15 catalyst.

However, under the reaction temperature of 250 °C and 100 vol% N$_2$, the toluene conversion of Cu$_1$Mn$_2$/SBA-15 was 64.8%, whereas the toluene conversion of Cu$_2$Mn$_1$/SBA-15 was only 14.5%, differing by 50.3%. It was concluded that the Cu/Mn molar ratio was the main factor influencing the toluene conversion in this case.

The Mn^{3+} and O$_{ads}$ concentrations decreased as the Cu/Mn mole ratio increased, and the toluene conversion increased with the increasing Mn^{3+} and O$_{ads}$ concentration. Amongst the catalysts studied, the Cu$_1$Mn$_2$/SBA-15 had the largest specific surface area and the active components were evenly distributed, which was conducive to improving the catalytic performance.[38] The Cu$_1$Mn$_2$/SBA-15 catalyst in this study had a toluene conversion of 68.5% at 250 °C, and this catalytic performance was comparable to that of precious metals (such as Ag),[39] while saving costs.

3.2.5. Stability of the catalyst. The effects of Cu$_1$Mn$_2$/SBA-15 on the stability of toluene conversion under 300 °C and an oxygen concentration of 25 vol% are shown in Fig. 11. The toluene conversion of Cu$_1$Mn$_2$/SBA-15 remained above 95% after a continuous reaction for 12 h, suggesting that the stability of Cu$_1$Mn$_2$/SBA-15 was excellent.

3.3 Catalytic combustion mechanism of toluene

3.3.1. Kinetic analysis. The kinetic analysis of Cu–Mn/SBA-15 for the toluene catalytic combustion consisted mainly of the calculation and analysis of the reaction rate, apparent activation

energy (E_a) and turnover frequency (TOF). The apparent E_a reflected the ease with which the reaction can proceed. The lower the apparent E_a, the easier the reaction will be. The TOF calculation gives an idea of the number of active sites on the catalyst surface and the intrinsic activity of the catalyst. The calculation method and formula of reaction rate, apparent E_a and TOF are as follows.

The reaction rate k (mol g$_{cat}{}^{-1}$ s^{-1}) can be calculated as follows:

$$k = \frac{\eta V}{W}$$

where η is the toluene removal efficiency (%), V is the toluene gas flow rate (mol s^{-1}), and W is the mass of catalyst (g).

The apparent E_a (kJ mol^{-1}) is calculated according to the Arrhenius formula:

$$\ln k = -\frac{E_a}{RT} + C$$

where R is the gas constant (8.314 J mol^{-1} K^{-1}), and T is the thermodynamic temperature (K).

The turnover frequency (TOF$_{Cu}$ or TOF$_{Mn}$) (s^{-1}) is given by:[40]

$$\text{TOF} = \frac{\eta V}{m/M}$$

where m is the mass of Cu or Mn (g), and M is the molar mass of Cu or Mn (g mol^{-1}).

Fig. 12 displays the reaction rates of the catalysts at different temperatures. It can be seen that the reaction rates of Cu–Mn/SBA-15 with different Cu/Mn molar ratios show a trend of continuous increase as the temperature increased. Among them, the reaction rate of toluene combustion catalyzed by Cu$_1$Mn$_2$/SBA-15 showed a positive correlation with the reaction temperature. In addition, for the toluene catalytic combustion by other Cu/Mn molar ratio catalysts, the relationship between the reaction rate and reaction temperature can be analyzed in two bands according to temperature. In the temperature range of 100–250 °C, the reaction rate increased slowly with increasing temperature. However, the reaction rate increased significantly as the temperature increased from 250 to 300 °C, which was consistent with the experimental results on the effect of temperature on toluene conversion.

Fig. 13 displays the Arrhenius plots of toluene combustion, and Table 4 lists the results of apparent E_a, reaction rate and TOF for different Cu/Mn molar ratio catalysts. The coefficients of determination (R^2) were all greater than 0.95, indicating that the model had a good fit. The apparent E_a of Cu$_1$Mn$_2$/SBA-15

(10.2 kJ mol^{-1}) was the minimum, which suggested that the toluene was more prone to combustion by Cu_1Mn_2/SBA-15. Meanwhile, the reaction rate of Cu_1Mn_2/SBA-15 (0.96 × 10^{-7} mol g$_{cat}^{-1}$ s^{-1}) was more than twice that of those of Cu_2Mn_1/SBA-15 and Cu_1Mn_1/SBA-15 under the same reaction conditions. The Cu_1Mn_2/SBA-15 also had the highest values of TOF$_{Cu}$ and TOF$_{Mn}$, indicating that it had an outstanding catalytic performance.

3.3.2. Catalytic combustion mechanism of toluene. It was of great significance to study the catalytic combustion mechanism of the VOCs on the catalysts to improve their catalytic combustion efficiency. The L–H mechanism model indicated that the reaction occurs between the adsorbed oxygen and the adsorbed VOCs molecules. The MVK mechanism model reaction step is manifested as the reaction of the VOC molecules with the O_{latt} in the catalyst. According to the experimental results of the effect of Cu–Mn/SBA-15 on the toluene removal efficiency at various reaction temperatures and concentrations of oxygen, it can be seen that increasing the concentration of oxygen revealed a remarkable effect on the improvement of toluene conversion for different catalysts in general. The XPS characterization results indicated that the main reason for the difference derived from the different contents of O_{ads} and O_{latt} in the catalysts. The effect of increasing the concentration of oxygen on toluene conversion for Cu_1Mn_2/SBA-15 was less than those of the other both catalysts. The higher O_{ads} content in Cu_1Mn_2/SBA-15 led to the L–H reaction mechanism that it mainly followed, and the oxygen species involved in the reaction were mainly O_{ads} species in the catalyst. For Cu_1Mn_1/SBA-15 and Cu_2Mn_1/SBA-15, the part of the reaction that follows the MVK mechanism increased due to their relatively high O_{latt} content. The increase of concentration of oxygen can accelerate the MVK mechanism reaction and improves the toluene conversion to some extent. In summary, the toluene catalytic combustion on Cu–Mn/SBA-15 followed both the MVK and L–H mechanisms, however, the proportion of both reaction mechanisms was different because of different the oxygen species content in the catalysts.

Fig. 14 shows the toluene reaction mechanism of Cu–Mn/SBA-15. Firstly, the toluene molecules are adsorbed on the surface of the catalyst, and then these adsorbed toluene molecules react with the O_{latt} in the catalyst to generate CO_2 and H_2O. Finally, the oxygen vacancy formed by the reaction is supplemented by gas phase oxygen. The reaction process described previously is the MVK mechanism. While the MVK mechanism reaction is taking place, the L–H mechanism reaction also takes place. This demonstrates that the gas phase oxygen can be adsorbed by the catalyst surface to form adsorbed oxygen, and then reacts with the toluene molecules adsorbed on the catalyst surface to generate CO_2 and H_2O.

4.   Conclusions

The Cu–Mn/SBA-15 catalysts with various loadings and the Cu/Mn mole ratios were produced using an impregnation method for exploring the effects of different reaction conditions on toluene conversion. The Cu_1Mn_2/SBA-15 showed the maximum catalytic performance for the toluene combustion at 300 °C because of the synergy between both the Cu and Mn and higher content of the Mn^{3+} and O_{ads}. Furthermore, the Cu_1Mn_2/SBA-15 also has the lowest apparent E_a, the highest reaction rate and the highest TOF content, all of which were conducive for the improvement of the toluene catalytic combustion. The toluene removal efficiency increased with the increase in reaction temperature, and the concentration of oxygen, and the increase of the concentration of oxygen showed a remarkable effect on the improvement of toluene removal efficiency, especially under a low reaction temperature (<250 °C). The toluene conversion could be improved by increasing the concentration of oxygen when the reaction temperature was relatively low. The toluene catalytic combustion for the Cu–Mn/SBA-15 followed both the MVK and L–H mechanism, but the proportion of both reaction mechanisms varied according to the content of O_{ads} and O_{latt} in the catalysts.

Conflicts of interest

There are no conflicts to declare.

Acknowledgements

References

1 A. He, J. Cheng, X. Zhang, M. Douthwaite, S. Pattisson and Z. Hao, *Chem. Rev.*, 2019, **119**, 4471–4568.

2 Y. Xu, Z. Qu, Y. Ren and C. Dong, *Appl. Surf. Sci.*, 2021, **560**, 149983.

3 C. Yang, G. Miao, Y. Pi, Q. Xia, J. Wu, Z. Li and J. Xiao, *Chem. Eng. J.*, 2019, **370**, 1128–1153.

4 A. Hamad and M. Fayed, *Chem. Eng. Res. Des.*, 2004, **82**, 895–906.

5 Y. Huang, S. S. H. Ho, Y. Lu, R. Niu, L. Xu, J. Cao and S. Lee, *Molecules*, 2016, **21**, 56.

6 K. M. R. S. H. MM, *Atmos. Environ.*, 2016, **140**, 117–134.

7 R. Li, L. Zhang, S. Zhu, S. Fu, X. Dong, S. Ida, L. Zhang and L. Guo, *Appl. Catal., A*, 2020, **602**, 117715.

8 A. M. Vandenbroucke, R. Morent, N. De Geyter and C. Leys, *J. Hazard. Mater.*, 2011, **195**, 30–54.

9 J.-L. Blin, L. Michelin, B. Lebeau, A. Naydenov, R. Velinova, H. Kolev, P. Gaudin, L. Vidal, A. Dotzeva, K. Tenchev and S. Todorova, *Catalysts*, 2021, **11**, 366.

10 S. Todorova, J. L. Blin, A. Naydenov, B. Lebeau, H. Kolev, P. Gaudin, A. Dotzeva, R. Velinova, D. Filkova, I. Ivanova, L. Vidal, L. Michelin, L. Josien and K. Tenchev, *Catal. Today*, 2020, **357**, 602–612.

11 X. Chen, Z. Zhao, Y. Zhou, Q. Zhu, Z. Pan and H. Lu, *Appl. Catal., A*, 2018, **566**, 190–199.

12 Y. Feng, L. Wei, Z. Wang, Y. Liu, H. Dai, C. Wang, H.-C. Hsi, E. Duan, Y. Peng and J. Deng, *J. Hazard. Mater.*, 2022, **439**, 129612.

13 J. Hu, X. Gao, Q. Fan and X. Gao, *RSC Adv.*, 2021, **11**, 16547–16556.

14 R. Fang, Z. Yang, X. Liu, Y. Yan, J. Ran and L. Zhang, *Fuel*, 2021, **286**, 119311.

15 J. Chen, X. Chen, W. Xu, Z. Xu, H.-p. Jia and J. Chen, *Appl. Catal., B*, 2018, **224**, 825–835.

16 P. N. H. Thi, N. C. Chien and N. D. M. Tuan, *RSC Adv.*, 2023, **13**, 13354–13364.

17 M. Li, W. Zhang, X. Zhang, Y. Lian, X. Niu and Y. Zhu, *J. Colloid Interface Sci.*, 2022, **630**, 301–316.

18 C. Xu, S. Dong, T. Chen, H. Liu, X. Zou, M. Ji, Z. Han, D. Shu, C. Wang and D. Chen, *Fuel*, 2023, **347**, 128401.

19 T. F. Garetto, E. Rincón and C. Apesteguıa, *Appl. Catal., B*, 2004, **48**, 167–174.

20 Q. Guo, Y. Liu, G. Qi and W. Jiao, *Energy*, 2019, **179**, 431–441.

21 J. Meng, F. Fang, N. Feng, H. Wan and G. Guan, *RSC Adv.*, 2020, **10**, 2472–2482.

22 L. Schick, R. Sanchis, V. González-Alfaro, S. Agouram, J. M. López, L. Torrente-Murciano, T. García and B. Solsona, *Chem. Eng. J.*, 2019, **366**, 100–111.

23 J.-L. Blin, L. Michelin, B. Lebeau, A. Naydenov, R. Velinova, H. Kolev, P. Gaudin, L. Vidal, A. Dotzeva and K. Tenchev, *Catalysts*, 2021, **11**, 366.

24 J. Hu, W. Li and R. Liu, *Catal. Today*, 2018, **314**, 147–153.

25 Y. Wang, D. Yang, S. Li, L. Zhang, G. Zheng and L. Guo, *Chem. Eng. J.*, 2019, **357**, 258–268.

26 J.-R. Li, W.-P. Zhang, C. Li, H. Xiao and C. He, *Appl. Surf. Sci.*, 2021, **550**, 149179.

27 Y. Zhang, Z. Zeng, Y. Li, Y. Hou, J. Hu and Z. Huang, *Fuel*, 2021, **288**, 119700.

28 P. Rayo, M. S. Rana, J. Ramírez, J. Ancheyta and A. Aguilar-Elguézabal, *Catal. Today*, 2008, **130**, 283–291.

29 S. Mo, Q. Zhang, J. Li, Y. Sun, Q. Ren, S. Zou, Q. Zhang, J. Lu, M. Fu and D. Mo, *Appl. Catal., B*, 2020, **264**, 118464.

30 Y. Ding, Q. Xian, E. Wang, X. He, Z. Jiang, H. Dan and W. Zhu, *New J. Chem.*, 2020, **44**, 13707–13715.

31 S. Hosseini, A. Niaei, D. Salari, M. C. Alvarez-Galvan and J. Fierro, *Ceram. Int.*, 2014, **40**, 6157–6163.

32 J.-R. Li, W.-P. Zhang, C. Li and C. He, *J. Colloid Interface Sci.*, 2021, **591**, 396–408.

33 H. Zhao, K. Fang, F. Dong, M. Lin, Y. Sun and Z. Tang, *J. Ind. Eng. Chem.*, 2017, **54**, 117–125.

34 Y. Luo, Y. Zheng, J. Zuo, X. Feng, X. Wang, T. Zhang, K. Zhang and L. Jiang, *J. Hazard. Mater.*, 2018, **349**, 119–127.

35 X. Zhang, J. Zhao, Z. Song, W. Liu, H. Zhao, M. Zhao, Y. Xing and H. Du, *J. Colloid Interface Sci.*, 2020, **562**, 170–181.

36 P. Wang, Y. He, Z. Yang, X. Liu, J. Ran and M. Guo, *ChemistrySelect*, 2020, **5**, 1122–1129.

37 S. Behar, P. Gonzalez, P. Agulhon, F. Quignard and D. Świerczyński, *Catal. Today*, 2012, **189**, 35–41.

38 Y. Qin, H. Wang, C. Dong and Z. Qu, *J. Catal.*, 2019, **380**, 21–31.

39 Y. Qin, Z. Qu, C. Dong and N. Huang, *Chin. J. Catal.*, 2017, **38**, 1603–1612.

40 Y. Luo, D. Lin, Y. Zheng, X. Feng, Q. Chen, K. Zhang, X. Wang and L. Jiang, *Appl. Surf. Sci.*, 2020, **504**, 144481.